



Contents lists available at ScienceDirect

# Journal of the Mechanical Behavior of Biomedical Materials

journal homepage: [www.elsevier.com/locate/jmbbm](http://www.elsevier.com/locate/jmbbm)

## 3D-printed biomaterials with regional auxetic properties



John J. Warner<sup>a</sup>, Allison R. Gillies<sup>b</sup>, Henry H. Hwang<sup>a</sup>, Hong Zhang<sup>a</sup>, Richard L. Lieber<sup>c,d</sup>,  
Shaochen Chen<sup>a,\*</sup>

<sup>a</sup> Department of NanoEngineering, University of California, San Diego, 9500 Gilman Drive, La Jolla, CA 92093, United States

<sup>b</sup> Department of Bioengineering, University of California, San Diego, 9500 Gilman Drive, La Jolla, CA 92093, United States

<sup>c</sup> Department of Orthopaedic Surgery, University of California, San Diego, 9500 Gilman Drive, La Jolla, CA 92093, United States

<sup>d</sup> Rehabilitation Institute of Chicago, 345 East Superior St, Chicago, IL 60611, United States

### ABSTRACT

Tissue engineering is replete with methods for inducing and mediating cell differentiation, which are crucial for ensuring proper regrowth of desired tissues. In this study, we developed a 3D-printed, non-positive Poisson's Ratio (NPPR) scaffold intended for future use in stretch-mediated cell differentiation applications, such as in muscle and tendon regeneration. We utilized dynamic optical projection stereolithography (DOPsL) to fabricate multi-layered, cell-laden NPPR scaffolds – these scaffolds can not only support aggregate cell growth, but can also be printed with locally-tunable force-displacement properties at length scales appropriate for tissue interaction. These NPPR multilayered mesh scaffolds can be embedded into highly elastic hydrogels in order to couple a reduced NPPR behavior to a normally Positive Poisson's Ratio (PPR) solid bulk material. This hybrid structure may potentially enable induced 'auxetic' behavior at the single-cell scale while tuning the Poisson's Ratio to a more isolated value. This would be uniquely suited for providing stretch-mediated effects for various cell-types within the tendon-to-muscle tissue transition.

### 1. Introduction

Auxetic structures and materials are those that have Negative Poisson's Ratios (NPR), which exhibit counter-intuitive behavior when force is applied: the transverse cross-sectional area increases with axial stretching (Liu and Hu, 2010; Shan et al., 2015). This is in contrast with the more intuitive deformation behavior of Positive Poisson's Ratio (PPR) materials, such as the common rubber band: PPR materials thin laterally as the material is stretched. However, auxetic architectures can be found naturally at various length scales, from crystalline unit-cell structures of certain metals and ceramics and macromolecular gas-infused polyurethane foams to engineered textile-scale weaves (Lubarda and Meyers, 1999; Yeganeh-Haeri et al., 1992; Liu, 2006). These architectures have two main defining features: unit-cells capable of movement, and internal void spaces. This applies to the cell/tissue scale as well – in order to build functionally robust auxetic architectures, unit-cell integrity must be maintained to facilitate displacement changes across the structure. With miniaturization, many solid structural elements either become too compliant or too brittle, both of which can contribute to structural integrity failure of auxetic unit-cell architecture. Conventionally, PPR materials are used in additive manufacturing processes, however careful structuring of PPR materials

enables Non-Positive Poisson's Ratio (NPPR) characteristics – during elongation, increases in length and width maintain or increase the effective cross-sectional area, while contraction causes the opposite effect. The auxeticity of these structures can be expressed as the negative ratio between transverse and axial elongation (Poisson's Ratio), and can vary via several factors, including unit-cell architecture, and the initial/final displacement states within the range of motion. This auxetic behavior is currently utilized in a wide variety of force-distribution industries, including impact-resistant vests, supportive clothing, and packing materials (Liu and Hu, 2010; Liu, 2006; McMullan et al., 2004), but also has applications in tissue engineering, as precise manipulation of forces and physical cues are crucial in affecting cell differentiation (Connelly et al., 2010).

Of interest is the tendon, the band of fibrous connective tissue that connects muscle to bone. Tendons are capable of withstanding large tensile stresses, a characteristic attributed to their polymeric helical sub-structures – these function similarly to coiled springs, and coupled interactions between them are thought to be responsible for the auxetic effect (Gatt et al., 2015; Thorpe et al., 2013). While other groups have discovered natural auxetic properties in tendons and vasculature (Marxen and Henkelman, 2003), our group has previously created auxetic 're-entrant' hydrogel structures to examine their effects on

\* Corresponding author.

E-mail address: [chen168@eng.ucsd.edu](mailto:chen168@eng.ucsd.edu) (S. Chen).

individual cells (Zhang et al., 2013), where emphasis was placed on equal transverse and axial elongation. In contrast, an artificial tendon structure might emphasize an auxetic ‘re-entrant’ design that mimics the aligned helical sub-structures of natural tendon. Regardless of the unit-cell design, these previous scaffolds were too small for clinical tissue replacement and the NPPR ranges were limited due to miniaturization-related fragility imposed by the polyethylene glycol diacrylate (PEGDA) hydrogel material used.

Synthetic and hybrid hydrogels are often used in biomaterial 3D-printing in efforts to mimic the native extracellular matrix (ECM) of mammalian cells. This trend of cellular environment recapitulation usually involves softer materials in the form of slabs matching configurations found in vivo. As hydrogels are soft and fragile, they are best suited in form factors resistant to collapse, such as bulk slabs, static structures, and larger-scale unit-cell structures. However, when miniaturizing these structures, ‘tougher’ materials are necessary to compensate for the compliance caused by reduced cross-sectional areas. Using a stiffer, more robust material with a fine macro-mesh architecture prevents structural collapse and enables translation of unit-cell forces over larger areas.

Previous work has been done to fabricate auxetic structures – on a smaller size scale, we previously utilized two-photon polymerization to fabricate auxetic PEGDA hydrogel meshes with  $\sim 16 \mu\text{m}$  unit-cell resolution. These scaffolds were too fragile to support their own weight in air, but provided an interesting observed cell behavior on synthetic auxetics – cells grown on these meshes were unable to complete the final phase of mitotic separation for unclear reasons (Zhang et al., 2013). One example of large size scale auxetic work comes from Clausen et al., who utilized dot-matrix printing to create auxetic structures with  $\sim 4 \text{ mm}$  unit-cells (Clausen et al., 2015). They recognized hydrogel fragility, and compensated by utilizing the more robust PDMS as a building material, and a rotational auxetic design. This previous work shows progressive improvement in material and design choices in constructing auxetic structures.

The goal of this work is to create auxetic scaffolds to aid in tendon-to-muscle tissue regeneration, i.e. appropriate scale for clinical tissue replacement, unit-cell architectures capable of supporting aggregate cell growth, and tunable auxetic kinematics with actuation and mechanical energy storage capabilities that mimic tendon behavior (Gatt et al., 2015; Ravary et al., 2004). Utilizing various unit-cell structures, a single scaffold can be imbued with different ‘stretch’ properties, which have been implicated in altering stem cell differentiation (Chen et al., 2013; Vanderhooft et al., 2009; Young and Engler, 2011; Zhou and Niklason, 2012). In this work, DOPsL is used in conjunction with a photopolymerizable polyurethane to optimize material strength, resolution, force translation, and scalability in fabricating auxetic scaffolds appropriate for muscle-tendon tissues.

## 2. Materials and methods

### 2.1. Photopolymer mixtures

BR-7432IG30 polyaliphatic urethane acrylate blend (30%/70%) with isobornyl acrylate (PAUA/IBOA) was donated by Biomar<sup>®</sup> as the photopolymerizable polyurethane. UV-absorber 2,2,6,6-tetramethylpiperidine 1-oxyl (TEMPO) was acquired from Sigma-Aldrich. Photoinitiator Bis(2,4,6-trimethylbenzoyl)-phenylphosphineoxide (Irgacure 819<sup>®</sup>) was acquired from Chiba. TEMPO was added to photocurable PAUA/IOBA prepolymer to 0.1% w/w in a loosely-capped, light-excluded tarred glass scintillation vial with magnetic stirbar. Irgacure 819 was then added to a final concentration of 2.0% w/w, then allowed to mix for another 6–12 h at room temperature.

### 2.2. DOPsL (Dynamic Optical Projection Stereolithography) setup

Fig. 1 shows our DOPsL printer, which features a digital micromirror device (DMD; DLP4000 from Texas Instruments), an ultraviolet light source (Omniscure S2000 with 320 nm filter), and a computer-

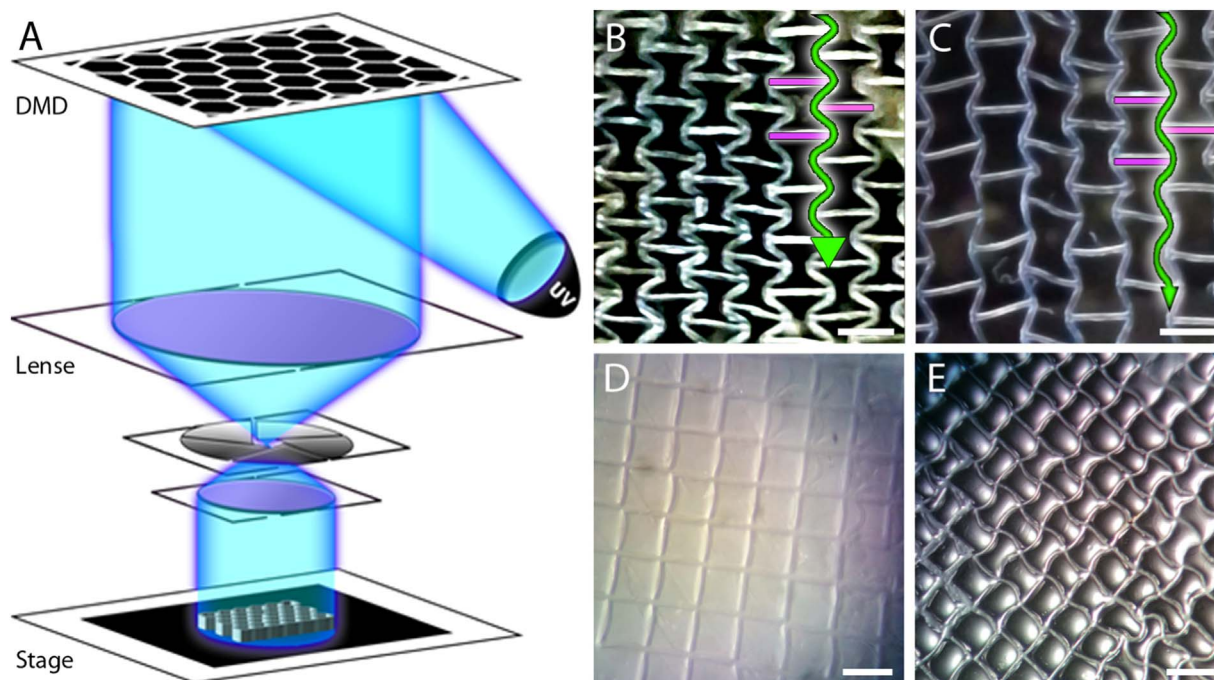


**Fig. 1.** (A) A schematic of the DOPsL setup: projected ultraviolet light is reflected and spatially-patterned via a digital micromirror device, and directed through condensation lenses onto a photosensitive prepolymer substrate. (B, C) Printed re-entrant auxetic mesh from PAUA/IBOA using a digital template optimized for hydrogels at large resolution and imaged at the extremes of the unit-cell range of motion. (B) The maximum compression boundary state just before mesh buckling. (C) The maximum elongation just before fractures appear. Despite both (B) and (C) marking boundary limits, both show extra unused unit-cell void space. (Green = z-line, purple = coupling elements at 2.2 mm). (D) PAUA/IBOA printed grid imaged in prepolymer. (E) Structure in image “D” washed with alcohol and filled with water shows contraction and self-arranged formation of a rotational auxetic. Scale bars are 2 mm. (For interpretation of the references to color in this figure legend, the reader is referred to the web version of this article.)

controlled stage (Newport), as described previously (Zhang et al., 2012). A computer-aided design program was used to construct a 3D object that was ‘sliced’ into 2D cross-sectional XY images, which were then transferred to the DMD. The DMD is composed of an array of approximately two million individually-addressable micromirrors, and UV light projected onto it can thus be spatially-patterned by toggling the micromirrors that correspond to the relevant regions of the desired image. By synchronizing the dynamic switching of the input images with the motion of the computer-controlled stage, fully 3D structures can be photopolymerized in seconds, thus allowing rapid prototyping of different mechanical features, such as strut thickness or hinge design. This also enables the construction of larger structures, achieved by breaking the desired structure into sequentially-printed ‘tiles’ – this expanded construction mode is limited only by stage movement, yet can still maintain 3.8  $\mu\text{m}$  resolution. The mesh constructs featured in this report are as large as 2 cm, yet retain 25  $\mu\text{m}$  wide struts.

Briefly, the photosensitive prepolymer solution is confined in the z-dimension with spacers or mechanized holders, then photopolymerized via the DOPsL system as described above. The nature of the material holder setup allows the system to be quickly fed with new prepolymer solution – normal operation can produce a PAUA/IBOA multilayer mesh in  $\sim 3$  min. Afterwards, the PAUA/IBOA construct is removed and soaked in chloroform for 5–10 min to remove excess viscous prepolymer, as well as any contaminating bacteria. The construct is then immediately submerged in  $\sim 100\%$  ethanol to mitigate any chloroform evaporation-induced shrinkage. Once equilibrated, the structure is removed from the ethanol, then rinsed with Milli-Q deionized water, and then placed in a sterile container until needed.

### 2.3. Finite analysis techniques

Finite element analysis (FEA) of hinge flexure regions was used to aid in refining micron-scale regions of the unit-cell. FEA was performed in Autodesk Inventor, with input material properties for BR-7432G130 (Segment Group, n.d.). Each model had strut dimensions of 45  $\mu\text{m}$   $\times$  160  $\mu\text{m}$   $\times$  80  $\mu\text{m}$  (W:L:D), where the bottom face was fixed, and a static analysis with 0.010 N force was applied. Allowed movement was confined within the plane. Using the Von Mises Stress (VMS) model for an isotropic viscoelastic material may limit FEA observations to pre-yield critical stress accumulation.

### 2.4. Cell culture and fluorescent staining

Two cell lines, a C3H/10T1/2 clone 8 Mus Musculus fibroblast line and a C3H/C2C12 Mus Musculus myoblast line, were thawed from cryopreservation and used at passages 18 and 3, respectively. Both cell lines were acquired from ATCC, cultured in growth medium (Gibco) Dulbecco's Modified Eagle's Medium (DMEM), and supplemented with 10% fetal bovine serum (Gibco). After reaching 80–90% confluence, the cells were passaged as follows: first, rinsed with 10 mL of sterile PBS buffer (Gibco), then treated with 1 mL of Trypsin-EDTA [0.25%], and incubated at 37  $^{\circ}\text{C}$  for 5–10 min. After lift-off, cells were resuspended in 5 mL of media, of which  $\sim 1$  mL of the resuspension volume was used in passaging 1 to 4–6 splits). For cell seeding, 5 mL resuspensions were centrifuged at 100g for 2 min, and after supernatant removal were resuspended in complete cell media to  $1 \times 10^3$  cells/ $\mu\text{L}$  for scaffold seeding. Cells were grown on scaffolds with complete media plus 1% pen/strep antibiotics. Cell-seeded scaffolds were rinsed with 3 mL of PBS for 1 min three times prior to staining. Live-dead staining was performed with LIVE/DEAD<sup>®</sup> Viability Kit L3224 (Life Technologies) using calcein AM and ethidium homodimer. 10T1/2 samples were fixed after staining. C2C12 cells were stained with Hoechst 33342 (Life Technologies) and rhodamine phalloidin (Biotium), and imaged immediately without fixing. Cell scaffolds were fixed at timepoint [day 22] with 4% paraformaldehyde in PBS for 20 min and permeabilized in 3% BSA, 0.1% Triton-X in PBS. A Leica fluorescent microscope with

image tiling capability was used for imaging.

#### 2.4.1. Scaffold preparation

During initial studies of the PAUA/IBOA's fibroblast adhesion capacity and cytotoxicity properties, bacterial contamination was observed for non-chloroform-treated samples despite treatment with 2% penicillin and streptomycin. Cells exposed to both unpolymerized and non-chloroform-treated PAUA/IBOA experienced bacterial contamination and slowed cell growth. Thus, it was decided that after DOPsL photopolymerization, all PAUA/IBOA scaffolds were to be soaked in chloroform for 5–10 min to remove contaminating bacteria, as well as any excess unpolymerized prepolymer. The construct was then immediately transferred to 100% ethanol to mitigate any chloroform evaporation-induced shrinkage, then rinsed with Milli-Q deionized water before transferring to a sterile container. The construct was then transferred to a sterile biological safety cabinet where 30  $\mu\text{L}$  of fibronectin (2  $\mu\text{g}/\text{mL}$ ) was added to the top face of the scaffold surface before placing the construct in vacuum for 30 min at room temperature; this was then repeated for the bottom face. The construct was then stored at room temperature for 30 min in sterile PBS with 2% penicillin and streptomycin followed by 24 h at 4  $^{\circ}\text{C}$ . Prior to seeding, the PBS was removed.

Cells were seeded directly atop the scaffold at  $\sim 2 \times 10^4$  via a 20  $\mu\text{L}$  volume of cell media (per ATCC guidelines) and allowed to sit on the scaffold for 30 min at 37  $^{\circ}\text{C}$  at 5%  $\text{CO}_2$ . After the allotted time, the scaffold was carefully flooded with warmed culture media supplemented with 1% penicillin and streptomycin. The samples were cultured in 12 and 24-well plates, and were gently transferred to new plates when cell growth on the bottom of the wells approached confluence ( $\sim 3$ –4 days). 10T1/2 cell lines were terminated after 12 days after confirming that the PAUA/IBOA + fibronectin scaffolds could facilitate cell adhesion, cell survival, and cell gap spanning potential.

#### 2.5. Mechanical actuation setup

For mechanical actuation testing, a scaffold was placed on a PDMS-lined petri dish, and a through-hole was made in the scaffold using a 25G needle. The scaffold was then transferred to a custom testing chamber filled with Milli-Q water, and allowed to sink (Lee et al., 2005). Any large air bubbles still attached to the scaffold were removed, then the scaffold was placed between a force transducer (Model 405A, Aurora Scientific, Aurora, ON, Canada) and an arm attached to a motorized micrometer (Model TRA12CC, Newport Corporation, Irvine, CA) by driving the device pins through the through-hole created earlier. The micrometer was adjusted until there was no visible slack in the scaffold, and until a minimal voltage deflection was detected with the force transducer; the pin-to-pin distance was then defined as the slack length ( $L_0$ ) of the scaffold. After establishing the slack length, the scaffold was stretched in 5%  $L_0$  increments until failure with three minutes of relaxation between stretches. Images of the scaffold were taken at the end of each stretch relaxation period with a Leica MZ16 stereomicroscope equipped with a Leica MC120 HD camera (Leica Microsystems, Buffalo Grove, IL). The overall scaffold strain was defined as  $(L - L_0)/L_0$ , where L is the pin-to-pin distance measured from the acquired images. The scaffold strain was not uniform within PPR and auxetic regions and therefore regional strains were measured by tracking two points within each region throughout the stretching protocol. Regional strains were calculated using the above equation applied to the two points within the specified region.

#### 2.6. Scanning electron microscopy

A field emission environmental microscope (FEI/Phillips XL30 ESEM FEG) was used to image the samples without fear of vacuum-induced shrinkage, as PAUA/IBOA is not a hydrogel. 10 kV was used for scattering mode images and 20–30 kV was used for backscattered

images. Though the PAUA/IBOA experienced mild charging, no sputter coat was required for scattered or backscattered images. UHV for 24 h was still used to prolong filament use, as well as a precaution against degassing of residual organics.

### 3. Results and discussion

Using our DOPsL platform, we constructed large form-factor and multi-layered meshes with tunable auxetic properties capable of supporting aggregate cell growth. DOPsL enables rapid and scalable tile-printing of structures while still retaining micron-scale resolution, which aided in iterating through design parameters such as structural thickness, material stiffness, and range of motion.

For the scaffold build material, an off-the-shelf photopolymerizable poly-aliphatic urethane-acrylate (PAUA) mixture BR-7432IG30 from Biomar® was used. The isobornyl acrylate (IBOA) component of this mixture acts as an incorporated plasticizer which enables more elastic deformation compared to pure PAUA. Like PDMS, PAUA/IBOA is easier to handle, flexible, and tolerates more strain per cross-sectional area as compared to many conventionally-printed hydrogels. These material properties impart enough flexibility for hinge functionality and unit-cell movement, but enough rigidity for preventing unit-cell collapse when fabricating smaller architectures.

Fig. 1B and C respectively show the maximum compression and extension states of a 3-tile re-entrant auxetic mesh scaffold printed using PAUA/IBOA. Scaffold actuation occurs along the horizontal coupling elements (purple) or the vertical accordion lines (green), but was actuated only along the latter. The accordion lines store energy in a spring-like manner, with force exerted laterally via the horizontal coupling elements. In the scaffold pictured in Fig. 1B and C, the range of motion between compressed and extended states is limited to a maximum axial change of 17.5% and a maximum transverse change of 21.1%. However, as can be seen from the images, the maximum compression and extension do not match expected behavior – full compression should result in no void space between the folded layers, and full extension should result in regular offset rectangles. Despite the appearance of sufficient space within the unit-cells for further movement, the scaffold buckles or fractures when pushed past the shown limits. This failure mode is apparent in Fig. 1B, as compression appears to cause bowing at the junctions between accordion lines and coupling elements, indicating excessive lateral force at the hinge-region. In the stretched state of Fig. 1C, some hinges appear to be ‘pinching,’ thus impeding complete extension of the accordion line. This auxetic design was previously optimized for hydrogels, and served as an initial design choice when transferring to the use of PAUA/IBOA, but as can be seen, still requires improvement – hydrogels are mechanically compliant soft materials, and thus despite having a lower tensile strength than PAUA/IBOA, are more tolerant of static printed hinge configurations even at larger scales. With this scaffold, the rigid PAUA/IBOA appears to exert more force on adjacent unit cells, as well as cause hinge inflexibility, thus compromising the range of motion. From these observations, it is clear that hinge designs that work for hydrogel-based scaffolds are not necessarily suitable for other materials, thus necessitating design changes.

As an initial design iteration, we printed a PAUA/IBOA scaffold to the same scale as the design seen in Fig. 1B and C, but without hinges, as can be seen in Fig. 1D. This iteration shows a thin-walled, 2 cm square-grid with sub-millimeter architecture immediately after printing. We then removed excess prepolymer and deposited 100  $\mu$ L of water on top – surface tension and unit-cell meniscus formation induced a 14.5% rotational contraction throughout the entire structure, thus self-arranging into a classic counter-rotational auxetic (CRA) design (Fig. 1E). This CRA structure was an interesting example of a system achieving auxeticity without explicitly defining auxetic structural features. However, while CRA-type designs have uniform auxeticity when undergoing elongation, they cannot effectively return to the same shape

unless exposed to cohesive surface tension, or printed in a pre-compressed state with shape memory materials – this is because compressive force actuation is ‘direct’ in nature, and not rotational; elongation only requires the structure to already be rotated. Though the CRA design may not be as useful for peripheral compression even when constructed from PAUA/IBOA, this iteration demonstrated that even regular unit-cell structures can self-arrange into auxeticity under the right circumstances. This informed our approach for the next iteration of design changes, namely requiring hinges and straight struts.

An ideal functional auxetic structure transmits force without collapsing into one continuous solid – this requirement increases in difficulty as length scales shrink, structural features such as struts become more fragile at micron scales. These features must possess some minimum rigidity in order to exert both compressive and tensile forces, a rationale that tends to favor more rigid materials such as polyurethanes instead of softer materials such as hydrogels. However, there exists a middle ground between the inflexibility that plagued the auxetic mesh shown in Fig. 1B, and the overly-compliant features that led to the regional collapse of the structure shown in Fig. 1E. For scaffolds fabricated as a single piece with no disparate components, the material must be able to function both as a rigid strut and as a flexible hinge where necessary. With DOPsL, this can be achievable by either patterning specific geometries and thicknesses, or affecting polymer cross-linking density. In this study, we relied only on modifying geometries and thicknesses to achieve the necessary rigidity and flexibility requirements. For NPPR auxetic meshes composed of a stiff, low shape-memory polymer such as PAUA/IBOA instead of a hydrogel, this necessitated architecture changes to improve unit-cell kinematics, namely via straight struts and hinges.

Using DOPsL, we printed a variant of the scaffold in Fig. 1B, this time thinning each strut to approximately a quarter of its original thickness (Fig. 2A) in hopes reducing the hinge inflexibility that caused the earlier buckling during compression. However, despite these thinner architectures, buckling was again observed during compression, followed by unit-cell fracturing as compression increased. This was caused by issues during fabrication – as DOPsL photopolymerizes structures, regions flanking the forming structures experience depletion of an in-solution free-radical inhibitor (TEMPO). These TEMPO-depleted regions overlap at junctions, making them more susceptible to non-specific autopolymerization (‘bleed’), and are visible as the dark shadows proximal to the hinge joints in Fig. 2A. Thus, these bleed-affected hinges were less flexible despite having thinner struts, experiencing both out-of-plane compressive buckling at internal angles below 30° and out-of-plane tensile deflections, eventually resulting in mechanical failure.

We utilized finite element analysis (FEA) of hinge flexure regions to aid in iterating unit-cell performance (Segment Group, n.d.). Fig. 2E shows a Von Mises Stress analysis of the acute hinge region with bleed seen in Fig. 2A. The simulation results show stress accumulation in the struts near the hinges – while this type of stress is less debilitating for structures composed of softer materials, excessive compression or extension will still induce strut failure instead of at the hinge. Indeed, FEA confirmed experimental observations of struts fracturing proximal to the hinge joint.

TEMPO-depleted bleed artifacts negatively affect build quality, and become more prevalent when decreasing length scales – attempts to miniaturize the acute-angle design directly ended up more severely flexing the struts. To correct for these bleed artifacts, we then modified the unit-cell architectures to include rounded corners that mitigated the effects of TEMPO-depleted regions. These Rounded Hinges (RH) have fewer bleed artifacts as can be seen in Fig. 2B (FEA-modeled in Fig. 2F), and actuation testing showed more unit-cell mobility during compression and axial elongation compared to the acute-angle design. This increased the overall range of motion and created a large, easy-to-handle, and functional auxetic mesh. However, when attempting to reduce the mesh 1/4 in scale, as seen in Fig. 2C, actuation testing of this

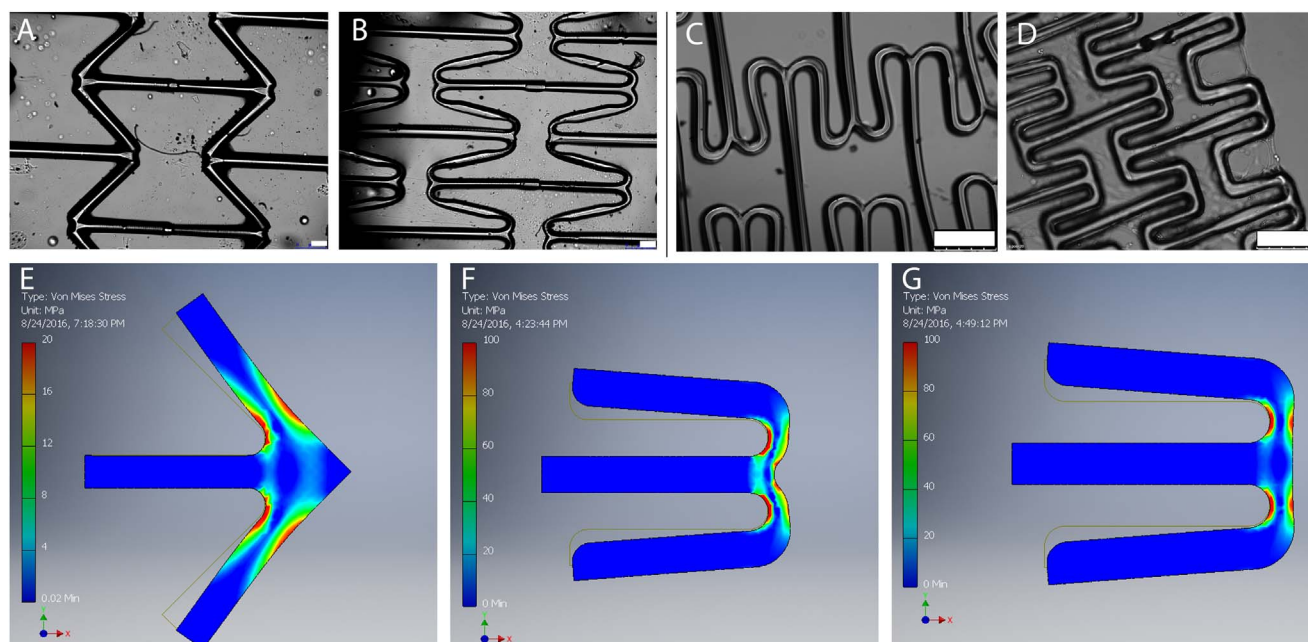


**Fig. 2.** Hinge design analysis. PAUA/IBOA unit-cell structures of a tiled mesh with A) large-scale acute hinge, B) large-scale rounded hinge, C) quarter-scale rounded hinge (RH), and D) fifth-scale stabilized-rounded hinge (SRH) configurations. Scale bars = 250  $\mu\text{m}$ . (E, F, G): FEA stress analysis of unit-cell hinge designs with observed bleed, used for informing iterative design. Scale bar of E is 0–20 MPa. Scale bar of F and G are 0–100 MPa.

smaller mesh revealed that these rounded hinges tended to pivot out-of-plane, causing the entire structure to become ‘wobbly’ and unstable. The results shown in Fig. 2F corroborate this, as the distribution of the force is along the majority of the bending region, thus creating a ‘wobbly’ hinge that increases range of motion at the expense of in-plane stability. This out-of-plane flexion was stabilized by creating a ‘Stabilized-Rounded’ Hinge (SRH), where we increased the cross-sectional area of the regions bracketing the hinge point, as seen in Fig. 2D (FEA-modeled in Fig. 2G). This stiffening of the neighboring regions localized the flexure point, thus providing better in-plane confinement while still compensating for bleed. This iterative design process demonstrates that our fabrication techniques, geometric features, and material bleed properties can all be leveraged to understand the limits of hinge-to-strut designs, allowing us to tune auxetic mesh kinematic behavior as we desire.

Using the RH and SRH concepts, we implemented them into individual, single-layer PAUA/IBOA meshes, as shown in Fig. 3A and B respectively. Each mesh’s auxetic region was flanked by non-auxetic honeycomb regions to enable uniform actuation, as well as to demonstrate that multiple stretching behaviors can be implemented in a single scaffold. The meshes were sufficiently robust to be handled and mechanically actuated - displacement maps were created through observed displacement in correlation with a force transducer as seen in the setup of an axially-offset multi-layered scaffold (Fig. 3C), and show that the overall stiffnesses of each mesh is tunable.

For the RH mesh shown in Fig. 3A, the middle auxetic region is characteristically soft, as shown by the steep slope of the localized strain (y-axis) vs. scaffold strain (x-axis). The middle auxetic region of the SRH mesh shown in Fig. 3B is, as expected, stiffer than that of the RH mesh, and can be inferred from the shallower displacement curve slope. Both RH and SRH structures showed better unit-cell range of motion than the original Acute Hinge structure shown in Figs. 1B and 2A. The SRH mesh showed improved handling, and was more effective at transmitting displacement throughout the structure than the RH mesh. Flexure in SRH was more localized to the hinge region, which minimized out-of-plane deflections compared to the RH mesh, which showed more unit-cell collapse and out-of-plane instability. The non-auxetic honeycomb regions are comparatively stiffer than the auxetic

regions, and elongate minimally along the longitudinal axis. Additionally, the non-auxetic honeycomb regions in the SRH mesh were thinned to match the cross-sectional area and feature size of the auxetic region. In the displacement map for the RH mesh (Fig. 3A), the honeycomb regions show almost no slope then fracture at a scaffold strain ratio of 0.2, whereas the SRH honeycombs fracture at the same strain ratio.

In considering an auxetic scaffold more conducive to tissue growth, we constructed an axially-offset, multi-layered SRH mesh structure as can be seen in Fig. 3C. Actuation testing of this multi-layered construct yielded a more robust displacement map, where mesh softness was retained in the auxetic region, and the honeycomb regions were revealed to be stiffer, as shown by the exponential curves. Scanning electron microscope images were taken to show more detail in the multi-layered SRH mesh (Fig. 3D), as well as a Zero Poisson’s Ratio (ZPR) mesh made utilizing the iterative principles learned in creating the SRH mesh.

To justify the use of these auxetic scaffolds as potential supportive structures in tendon-to-muscle tissue engineering, we conducted in vitro cell culture studies with relevant fibroblast and myoblast cell lines. To prepare these scaffolds for cell culture, physisorbed fibronectin was used as a coating to enable cell adhesion. As fibroblasts and myotubes constitute the majority cell types found in myotendinous junction, we cultured 10T1/2 fibroblast cells and C2C12 myoblast cells on single-layer and multi-layer meshes, as well as both auxetic and Zero Poisson’s Ratio behaviors. With the multi-layer meshes, we implemented 1/2 unit-cell offsets between layers, to enhance cellular integration with the scaffolds. Additionally, as each layer was constructed to be only 80  $\mu\text{m}$  thick, we ensured that the multi-layer scaffolds were below the 250  $\mu\text{m}$  diffusion limit recommended for static cell culture (Lee et al., 2005).

As can be seen from Fig. 4, cell culture results indicate that the polymerized, fibronectin-coated PAUA/IBOA auxetic scaffolds are capable of supporting aggregate cell growth. Fig. 4A and B demonstrate cellular adhesion capacity – Fig. 4A shows murine fibroblasts adhering to a planar face on a single-layer SRH mesh, and Fig. 4B shows mid-structure cell profiles adhering laterally to the strut’s sidewalls, also on a single-layer SRH mesh. Fig. 4C shows that murine myoblasts are even

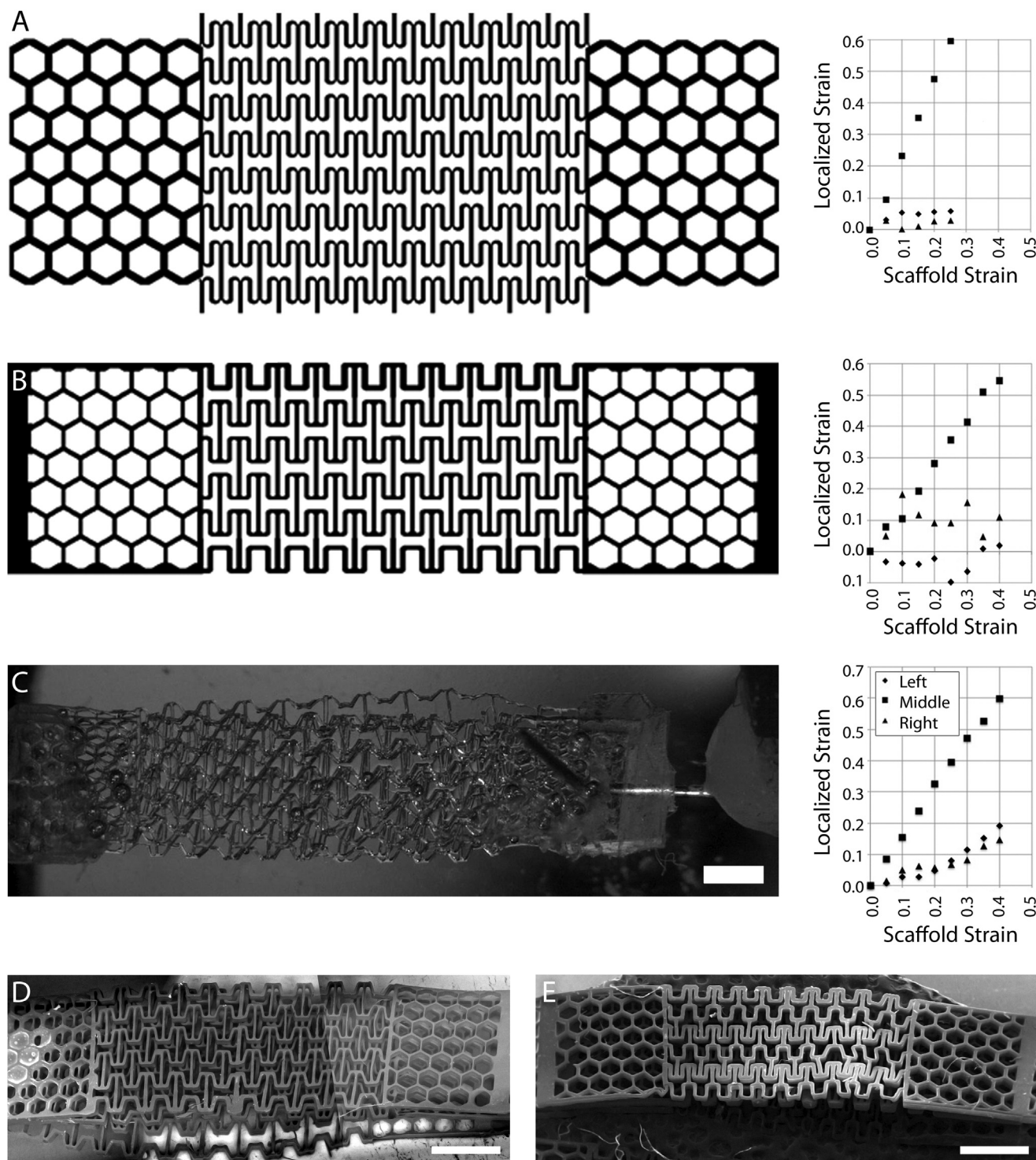


**Fig. 3.** Design tunability of tile-printed PAUA/IBOA mesh structures and corresponding scaffold strain and localized strain: The local incremental stretch displacements of the respective scaffolds changes with hinge-design (A-ROUNDED, B-STABILIZED ROUNDED single-layer digital templates). RIGHT: scaffold strain vs. localized strain of the respective meshes. (◆ = left honeycomb PPR region, ▲ = right honeycomb PPR region, ■ = middle auxetic region) C) shows an offset multilayer on the stretch device, D and E) SEM images show unit structure flexibility and application to produce offset unit cells for tissue in NPR and zero PR configurations. Scale bar = 1 mm.

capable of spanning void spaces in a single-layer SRH mesh as large as 250 μm in 3 weeks. However, void space elimination is possible with preservation of reduced auxetic behavior, through implementing these NPPR mesh scaffolds as internal structural skeletons within highly elastic hydrogels (Supplementary information). Fig. 4D shows mild cell death that could be improved with a ‘greener’ polyurethane material in future works (Pyo et al., 2011). These scaffolds were all seeded at a density of  $2 \times 10^4$  cells/structure. Fig. 4E depicts surface imaging of a

multi-layer SRH mesh seeded with myoblasts and stained for F-actin and nuclei, where the cells appear to be wrapping transverse to the axial direction along individual struts, forming a surface mat of cells. This behavior has been observed previously with cells undergoing stretching (Dalby et al., 2007). However, deeper imaging of the multi-layer scaffold as shown in Fig. 4F shows nuclear-stained cells appearing to spread along the unit-cells’ internal walls and normal to the planar surface. Thus, we demonstrate that the auxetic scaffolds are capable of

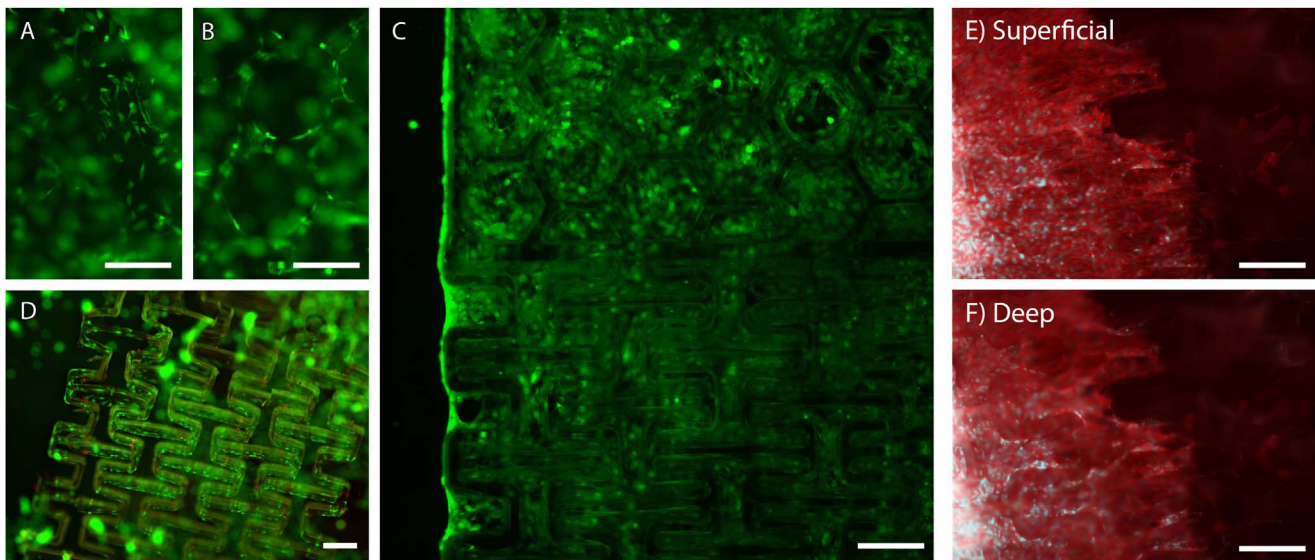


**Fig. 4.** Cell viability and location assessment on PAUA/IBOA scaffolds. A) surface adhesion of fibroblasts at day 5. B) internal wall adhesion of fibroblasts at day 5. C) gap-spanning myoblasts filling single-layer SRH mesh at week 3. D) live-dead of fibroblasts on single-layer SRH mesh at day 5: Live (green) = calcein AM; Dead (red) = ethidium bromide. E) multi-layer zero Poisson with myoblasts at week 3, F) multi-layer zero Poisson cell penetration evidence at  $\sim 80 \mu\text{m}$  or midway through the first layer. F-actin (Red) = phalloidin, Nuclear (Cyan) = Hoechst. Scale bars =  $250 \mu\text{m}$ . (For interpretation of the references to color in this figure legend, the reader is referred to the web version of this article.)

sustaining cellular growth and preserving gap spanning capability between layer interfaces, thus potentially acceptable for tissue formation.

#### 4. Conclusion

In this study, we used our DOPsL system to fabricate multi-layered, Non-Positive Poisson's Ratio meshes, integrating them into a single cell-supporting scaffold for tissue engineering applications. By utilizing the DOPsL system's pattern flexibility, tiling functionality, and iterative speed, we were able to construct robust tissue-scale scaffolds with auxetic properties that were tunable through adjusting fabrication parameters. Our observations of unit-cell mesh actuation were consistent with FEA modeling, which helped tune the hinge and strut modifications necessary for proper scaffold actuation. Future work will be needed to optimize our auxetic meshes as a platform for stretch-mediated differentiation and eventually, facilitating tendon-muscle tissue regeneration.

#### Acknowledgements

The project described was supported, in part, by the California Institute for Regenerative Medicine (RT3-07899), National Science Foundation (CMMI-1332681 and CMMI-1547005), National Skeletal Muscle Research Center NIH grants (R24HD050837, R01EB021857, and R21HD090662) and UCSD Neuroscience Microscopy Shared Facility Grant P30 NS047101. Additionally, we thank the UCSD Nanoengineering Materials Research Center for use of SEM imaging equipment and Shannon Bremmer, Helen Bae, Pengrui Wang, Sabine Faulhaber, and Wayne Neilson for their valuable assistance. We have special appreciation and thanks for Marc Meyers's and his research in molecular level auxetics, acknowledging that his contributions provide a foundation and influenced our work, even years later, in implementing auxetic behavior at the macro-engineered level for biomedical materials.

#### Appendix A. Supplementary material

Supplementary data associated with this article can be found in the online version at <http://dx.doi.org/10.1016/j.jmbbm.2017.05.016>.

#### References

- Chen, Q., Liang, S., Thouas, G.A., 2013. Elastomeric biomaterials for tissue engineering. *Prog. Polym. Sci.* 38 (3–4), 584–671. <http://dx.doi.org/10.1016/j.progpolymsci.2012.05.003>.
- Clausen, A., Wang, F., Jensen, J.S., Sigmund, O., Lewis, J.A., 2015. Topology optimized architectures with programmable Poisson's ratio over large deformations. *Adv. Mater.* 27 (37), 5523–5527. <http://dx.doi.org/10.1002/adma.201502485>.
- Connelly, J.T., Gautrot, J.E., Trappmann, B., Tan, D.W.-M., Donati, G., Huck, W.T.S., Watt, F.M., 2010. Actin and serum response factor transduce physical cues from the microenvironment to regulate epidermal stem cell fate decisions. *Nat. Cell Biol.* 12 (7), 711–718. <http://dx.doi.org/10.1038/ncb2074>.
- Dalby, M.J., Gadegaard, N., Tare, R., Andar, A., Riehle, M.O., Herzyk, P., Wilkinson, C.D., Oreffo, R.O., 2007. The control of human mesenchymal cell differentiation using nanoscale symmetry and disorder. *Nat. Mater.* 6 (12), 997–1003. <http://dx.doi.org/10.1038/nmat2013>.
- Gatt, R., Vella Wood, M., Gatt, A., Zarb, F., Formosa, C., Azzopardi, K.M., Casha, A., Agius, T.P., Schembri-Wismayer, P., Attard, L., et al., 2015. Negative Poisson's ratios in tendons: an unexpected mechanical response. *Acta Biomater.* 24, 201–208. <http://dx.doi.org/10.1016/j.actbio.2015.06.018>.
- Lee, M., Dunn, J.C.Y., Wu, B.M., 2005. Scaffold fabrication by indirect three-dimensional printing. *Biomaterials* 26 (20), 4281–4289. <http://dx.doi.org/10.1016/j.biomaterials.2004.10.040>.
- Liu, Q., 2006. Literature review: materials with negative poisson's ratios and potential applications to aerospace and defence. *Aust. Gov. Dep. Def.* 1–47.
- Liu, Y., Hu, H., 2010. A review on auxetic structures and polymeric materials. *Sci. Res. Essays* 5 (10), 1052–1063.
- Lubarda, V., Meyers, M., 1999. On the negative poisson ratio in monocrystalline zinc. *Scr. Mater.* 40 (8), 975–977. [http://dx.doi.org/10.1016/S1359-6462\(99\)00039-1](http://dx.doi.org/10.1016/S1359-6462(99)00039-1).
- Marxen, M., Henkelman, R.M., 2003. Branching tree model with fractal vascular resistance explains fractal perfusion heterogeneity. *Am. J. Physiol. Heart Circ. Physiol.* 284 (5), H1848–H1857. <http://dx.doi.org/10.1152/ajpheart.00510.2002>.
- McMullan, P.J., Kumar, S., Griffin, A.C., 2004. Textile Fibers Engineered From Molecular Auxetic Polymers.
- Pyo, S.-H., Persson, P., Mollaahmad, M.A., Sørensen, K., Lundmark, S., Hatti-Kaul, R., 2011. Cyclic carbonates as monomers for phosgene- and isocyanate-free polyurethanes and polycarbonates. *Pure Appl. Chem.* 84 (3), 637–661. <http://dx.doi.org/10.1351/PAC-CON-11-06-14>.
- Ravary, B., Pourcelot, P., Bortolussi, C., Konieczka, S., Crevier-Denoix, N., 2004. Strain and force transducers used in human and veterinary tendon and ligament biomechanical studies. *Clin. Biomech.* 19 (5), 433–447. <http://dx.doi.org/10.1016/j.clinbiomech.2004.01.008>.
- Segment Group, M., n.d., UV/EB OLIGOMERS BR-7432GB Product Data Sheet Bomar® BR-7432GB Aliphatic Difunctional Urethane Acrylate Oligomer.
- Shan, S., Kang, S.H., Zhao, Z., Fang, L., Bertoldi, K., 2015. Design of planar isotropic negative Poisson's ratio structures. *Extrem. Mech. Lett.* 4, 96–102. <http://dx.doi.org/10.1016/j.eml.2015.05.002>.
- Thorpe, C.T., Klemm, C., Riley, G.P., Birch, H.L., Clegg, P.D., Screen, H.R.C., 2013. Helical sub-structures in energy-storing tendons provide a possible mechanism for efficient energy storage and return. *Acta Biomater.* 9 (8), 7948–7956. <http://dx.doi.org/10.1016/j.actbio.2013.05.004>.
- Vanderhoof, J.L., Alcoutlabi, M., Magda, J.J., Prestwich, G.D., 2009. Rheological

- properties of cross-linked hyaluronan-gelatin hydrogels for tissue engineering. *Macromol. Biosci.* 9 (1), 20–28. <http://dx.doi.org/10.1002/mabi.200800141>.
- Yeganeh-Haeri, A., Weidner, D.J., Parise, J.B., 1992. Elasticity of  $\alpha$ -Cristobalite: a silicon dioxide with a negative Poisson's ratio. *Science* (80-) 257 (5070), 650–652. <http://dx.doi.org/10.1126/science.257.5070.650>.
- Young, J.L., Engler, A.J., 2011. Hydrogels with time-dependent material properties enhance cardiomyocyte differentiation in vitro. *Biomaterials* 32 (4), 1002–1009. <http://dx.doi.org/10.1016/j.biomaterials.2010.10.020>.
- Zhang, C.A.P., Qu, X., Soman, P., Hribar, K.C., Lee, J.W., Chen, S., He, S., 2012. Rapid fabrication of complex 3D extracellular microenvironments by dynamic optical projection stereolithography. *Adv. Mater.* (24), 4266–4270. <http://dx.doi.org/10.1002/adma.201202024>.
- Zhang, W., Soman, P., Meggs, K., Qu, X., Chen, S., 2013. Tuning the Poisson's ratio of biomaterials for investigating cellular response. *Adv. Funct. Mater.* 23 (25), 3226–3232. <http://dx.doi.org/10.1002/adfm.201202666>.
- Zhou, J., Niklason, L.E., 2012. Microfluidic artificial “vessels” for dynamic mechanical stimulation of mesenchymal stem cells. *Integr. Biol.* 4 (12), 1487–1497. <http://dx.doi.org/10.1039/C2IB00171C>.